



**UNIVERSITY OF LEEDS**

This is a repository copy of *Spatio-temporal atlas of bone mineral density ageing*.

White Rose Research Online URL for this paper:

<http://eprints.whiterose.ac.uk/145304/>

Version: Accepted Version

---

**Proceedings Paper:**

Farzi, M, Pozo, JM, McCloskey, E et al. (3 more authors) (2018) Spatio-temporal atlas of bone mineral density ageing. In: Lecture Notes in Computer Science. International Conference on Medical Image Computing and Computer-Assisted Intervention: MICCAI 2018, 16-20 Sep 2018, Granada, Spain. Springer Verlag , pp. 720-728. ISBN 9783030009274

[https://doi.org/10.1007/978-3-030-00928-1\\_81](https://doi.org/10.1007/978-3-030-00928-1_81)

---

© Springer Nature Switzerland AG 2018. This is an author produced version of a conference paper published in Lecture Notes in Computer Science. Uploaded in accordance with the publisher's self-archiving policy.

**Reuse**

Items deposited in White Rose Research Online are protected by copyright, with all rights reserved unless indicated otherwise. They may be downloaded and/or printed for private study, or other acts as permitted by national copyright laws. The publisher or other rights holders may allow further reproduction and re-use of the full text version. This is indicated by the licence information on the White Rose Research Online record for the item.

**Takedown**

If you consider content in White Rose Research Online to be in breach of UK law, please notify us by emailing [eprints@whiterose.ac.uk](mailto:eprints@whiterose.ac.uk) including the URL of the record and the reason for the withdrawal request.



[eprints@whiterose.ac.uk](mailto:eprints@whiterose.ac.uk)  
<https://eprints.whiterose.ac.uk/>

# Spatio-Temporal Atlas of Bone Mineral Density Ageing

Mohsen Farzi<sup>1,2</sup>, Jose M. Pozo<sup>1</sup>, Eugene McCloskey<sup>2</sup>, Richard Eastell<sup>2</sup>, J. Mark Wilkinson<sup>2</sup>, and Alejandro F. Frangi<sup>1</sup>

<sup>1</sup> Centre for Computational Imaging & Simulation Technologies in Biomedicine (CISTIB), University of Sheffield, Sheffield, UK

<sup>2</sup> Academic Unit of Bone Metabolism, University of Sheffield, Sheffield, UK

**Abstract.** Osteoporosis is an age-associated bone disease characterised by low bone mass. An improved understanding of the underlying mechanism for age-related bone loss could lead to enhanced preventive and therapeutic strategies for osteoporosis. In this work, we propose a fully automatic pipeline for developing a spatio-temporal atlas of ageing bone. Bone maps are collected using a dual-energy X-ray absorptiometry (DXA) scanner. Each scan is then warped into a reference template to eliminate morphological variation and establish a correspondence between pixel coordinates. Pixel-wise bone density evolution with ageing was modelled using smooth quantile curves. To construct the atlas, we amalgamated a cohort of 1714 Caucasian women (20-87 years) from five different centres in North Western Europe. As a systematic difference exists between different DXA manufacturers, we propose a novel calibration technique to homogenise bone density measurements across the centres. This technique utilises an alternating minimisation technique to map the observed bone density measurements into a latent standardised space. To the best of our knowledge, this is the first spatio-temporal atlas of ageing bone.

## 1 Introduction

Ageing is associated with a gradual and progressive bone loss, which predisposes to osteoporosis. Osteoporosis is a bone disease characterised by low bone mass and micro-architectural deterioration. Given the close relationship between involutional bone loss and the underlying mechanism of osteoporosis, improving the understanding of the bone ageing process has been of interest for the osteoporosis research community [1, 2]. To facilitate this understanding, we propose a method to develop a spatio-temporal atlas of ageing bone in the femur.

Spatio-temporal atlases are useful tools for visualising and accessing a wide range of data in Medical Image Computing. For example, brain atlases demonstrated great potential for visualising age-related pathology in Alzheimer’s disease [3]. However, to the best of our knowledge, no bone ageing atlas has been developed in osteoporosis research so far. Developing a comprehensive model of involutional bone loss is a challenging task. Firstly, this requires a robust and accurate quantification technique for bone mineral density (BMD) measurement

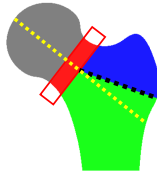


**Fig. 1:** Region Based Analysis. BMD values are averaged in the specified ROIs; The neck, trochanteric, and inter-trochanteric regions are shown in red, blue, and green.

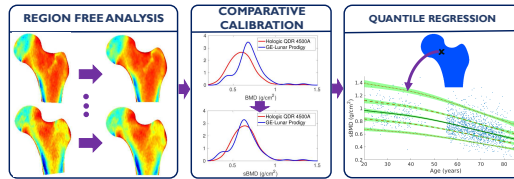


**Fig. 2:** Bone Ageing Analysis Pipeline. BMD maps are warped into a reference template to eliminate morphological variations. Cross-calibration between different DXA manufacturers is established to homogenise BMD measurements. Smooth quantile curves are fitted to the standardised BMD values at each pixel coordinate.

and its spatial distribution. Dual-energy X-ray Absorptiometry (DXA) is the reference gold standard to measure BMD in clinical practice [4]. In conventional DXA analysis, BMD values are averaged in *a priori* specified Regions of Interest (ROIs) to compensate for shape variation between scans (Fig. 1). This data averaging, however, may reduce our insight on more focal BMD deficits. The second challenge is the ability to homogenise BMD across different technologies, as a systematic difference exists between different DXA manufacturers [5, 6].

We address these challenges as follows: To maintain fidelity to high-resolution pixel BMD values, we develop a group-wise image warping technique termed region free analysis (RFA). This image warping eliminates the morphological variation between scans and establishes a correspondence between pixel coordinates. Farzi et al. presented a similar approach to analysing periprosthetic BMD change [7]. However, their method is semi-automatic and is not applicable to large-scale datasets. To amalgamate data from different scanner technologies, we propose a novel cross-calibration technique by minimising the mutual difference between the BMD probability distributions measured by each proprietary DXA scanner.

This paper describes the development of the first spatio-temporal atlas of ageing bone in the femur. To this end, we propose a fully automatic pipeline to ensure high-throughput computing applicable to large-scale datasets (Fig. 2). We also derive a set of reference quantile curves per each pixel to model the BMD evolution with ageing. The developed atlas provides new insights into the spatial pattern of bone loss, for which the conventional DXA analysis is insensitive.

## 2 Methods

### 2.1 Preprocessing

The raw data from a DXA scanner is not immediately usable for analysing BMD maps. To export BMD maps, the raw data requires processing using a computer software package specific to its vendor. We used Apex v3.2 and Encore v16 to extract pixel BMD information for Hologic Inc. (Waltham, MA) and GE-Lunar Corp. (Madison, WI) scanners, respectively.

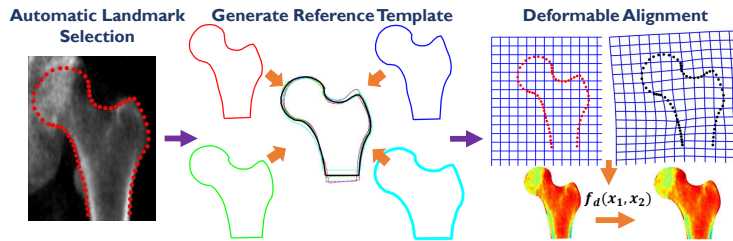


**Fig. 3:** Region Free Analysis. Sixty-five landmark points are automatically selected. A reference shape is learned using generalised Procrustes analysis. Each scan is warped to the template using a thin plate spline (TPS) registration.

## 2.2 Region Free Analysis

RFA aims to find a set of coordinate transformations such that the warped scans are aligned with each other in the template domain (Fig. 3). This warping allows pixel level inference at each coordinate in the template domain.

**Automatic Landmark Extraction:** Statistical shape models (SSMs) are a robust and accurate approach to automatically locate and segment the femur in radiographic imaging [8]. Here, we used a software package, called *BoneFinder*, to automatically select 65 controlling landmark points around the femur.

**Template Generation:** Generalised Procrustes analysis is utilised to find the reference template [9]. First, all scans are aligned to a common position, scale, and orientation. Next, the reference template is updated as the average of the aligned shapes. The algorithm iterates between these two steps until convergence.

**Pairwise Registration:** To eliminate morphological variation between scans, each individual scan is warped to the template domain using a thin plate spline (TPS) registration technique [10]. Since image resolution varies between different manufacturers, the space grid at the template domain was set to the finest resolution available, i.e.  $0.25 \times 0.25 \text{ mm}^2$ .

## 2.3 Quantile Regression

Assume the real-valued random variable  $X$  with the cumulative distribution function (CDF)  $F_X(x) = P(X \leq x)$  represents a response variable of interest, e.g. BMD at one pixel coordinate, and the real-valued random variable  $T$  represents an explanatory covariate, e.g. age. Then, the conditional quantile function  $(u, t) \mapsto Q_{X|T}(u, t)$  is defined as

$$Q_{X|T}(u, t) := \inf \{x : u \leq F_{X|T=t}(x)\}. \quad (1)$$

For fitting the quantile curves from scattered points  $\{(x_n, t_n)\}_{n=1}^N$ , we deployed the R-package 'VGAM' using the LMS technique [11]. In this technique, a Box-Cox transformation of the response variable  $X$  with parameters  $\lambda$ ,  $\mu$ , and  $\sigma$  is applied to obtain normality, i.e.  $Z = \psi_{\mu, \sigma, \lambda}(X)$ . Given that  $Q_Z(u)$  is known

for a normal distribution, if smooth curves  $\lambda(t)$ ,  $\mu(t)$ , and  $\sigma(t)$  are estimated, then  $Q_{X|T}(u, t)$  can be simply estimated using the inverse transformation, i.e.  $Q_{X|T}(u, t) = \psi_{\mu(t), \sigma(t), \lambda(t)}^{-1}(Q_Z(u))$ .

The smoothness of the fitted parameter curves is controlled using a vector smoothing spline. We modelled  $\lambda(t)$  and  $\sigma(t)$  as intercept terms and  $\mu(t)$  as a smooth function with the equivalent degree of freedom 3. To assess the precision of the estimated quantile curves, we used a bootstrapping procedure. We randomly sampled subjects with replacement and re-estimated the quantile curves. We repeated this procedure 1000 times collecting a distribution of possible quantile curves. From these observations, we estimated the confidence intervals at 5% significance level [12].

## 2.4 Comparative Calibration

Assume the latent random variable  $X$  represents the underlying true BMD values and the random variable  $Y^c$  represents the observed BMD values measured on the machine  $c$ . Lu et al. proposed a linear model for comparative calibration between DXA scanners [6].

$$Y^c = a_c X + b_c + \epsilon_c. \quad (2)$$

$\epsilon_c \sim \mathcal{N}(0, \sigma_c^2)$  represents the measurement noise of scanner  $c$ . Lue et al. [6] proposed an expectation maximisation (EM) approach to estimate the model parameters  $\{a_c, b_c, \sigma_c\}_{c=1}^C$  using BMD measurements based on a common group of individuals. This method cannot be used if everyone is scanned only once on each machine and no repeated measurements are available. Requiring repeated measurements of each subject across all machines is an implausible assumption in large-scale multi-centre studies. Alternatively, calibration against phantom measurements is a common pragmatic approach. However, using human measurements is preferred for calibration purposes as a significant disagreement exists between the model parameters fitted to the phantom measurements and those fitted to the human measurements [5].

Here, we propose a novel calibration technique based on human measurements where no repeated measurements are required (cf. [6]). The new technique is developed based on two assumptions. First, a unique distribution of BMD values exists independent of the manufacturers. Assuming different cohorts measured on different scanners are sampled from the same population, the estimated distributions of calibrated BMD values should match one another. Second, the signal to noise ratio is sufficiently large such that

$$Q_{Y^c}(u) \approx a_c Q_X(u) + b_c. \quad (3)$$

Note that if the noise power is zero, then the approximation would be replaced with equality in Eq. 3. With this assumption, estimation of the model parameters  $\Theta = \{a_c, b_c\}$  can be decoupled from the estimation of noise variances, i.e.  $\{\sigma_c^2\}$ .

The parameters  $\Theta$  are estimated by minimizing the cost function

$$\mathcal{J} = \frac{1}{2} \sum_{c=1}^C \int_0^1 (Q_{Y^c}(u) - a_c Q_X(u) - b_c)^2 du, \quad (4)$$

including the latent variable  $X$ . This minimum has two degrees of freedom. More precisely, if  $a_c^*$  and  $b_c^*$  minimise the cost  $\mathcal{J}$  for an  $X$ , then  $a'_c = \alpha a_c^*$  and  $b'_c = \beta a_c^* + b_c^*$  minimise the cost as well for a corresponding linear transformation of  $X$  by any arbitrary  $\alpha \neq 0$  and  $\beta$ . To resolve this ambiguity, we define the true BMD as the average of expected observations given the latent variable  $X$ , i.e.  $X = \frac{1}{C} \sum_c E(Y^c|X)$ . This results in the two constraints

$$\sum_c b_c = 0 \quad \text{and} \quad \frac{1}{C} \sum_c a_c = 1. \quad (5)$$

**Optimisation:** To convert the constrained optimization problem into an unconstrained one, we can simply express the parameters  $a_C$  and  $b_C$  based on the other parameters:  $a_C = C - \sum_{c \neq C} a_c$  and  $b_C = -\sum_{c \neq C} b_c$

To estimate the parameters, an alternating minimisation technique is adopted: Given the model parameters, the latent variable  $x_n$  for each of the  $N$  scanned subjects can be estimated as (step 1),

$$x_n = E(X|y_n^{c_n}; a_{c_n}, b_{c_n}) \approx \frac{1}{a_{c_n}} (y_n^{c_n} - b_{c_n}), \quad (6)$$

where  $c_n$  is the corresponding machine. To update the model parameters, we set the gradients  $\frac{\partial}{\partial a_c} \mathcal{J}$  and  $\frac{\partial}{\partial b_c} \mathcal{J}$  to zero.

$$\begin{aligned} \frac{\partial}{\partial a_c} \mathcal{J} &= (a_c + \sum_{c' \neq C} a_{c'} - C) \int_0^1 Q_X(u)^2 du + (b_c + \sum_{c' \neq C} b_{c'}) \int_0^1 Q_X(u) du \\ &\quad + \int_0^1 Q_X(u) (Q_{Y^C}(u) - Q_{Y^c}(u)) du = 0, \end{aligned} \quad (7)$$

$$\begin{aligned} \frac{\partial}{\partial b_c} \mathcal{J} &= (a_c + \sum_{c' \neq C} a_{c'} - C) \int_0^1 Q_X(u) du + (b_c + \sum_{c' \neq C} b_{c'}) \\ &\quad + \int_0^1 (Q_{Y^C}(u) - Q_{Y^c}(u)) du = 0. \end{aligned} \quad (8)$$

Computing  $Q_X(u)$  from step 1, Eq. 7 and Eq. 8 are linear with respect to the model parameters. Hence, we have  $2(C-1)$  linear equations with  $2(C-1)$  parameters for which a closed-form solution exists (step 2). The algorithm iterates between these two steps until the  $\ell_2$ -norm of the difference between estimated parameters at two consecutive iterations is less than a user-defined tolerance  $\epsilon$ .

### 3 Results and Experiments

To construct atlas, we used  $N = 1714$  femoral scans (left side) of women aged 20-87 years collected as part of the Osteoporosis and Ultrasound study (OPUS)

[13]. Five centres were involved in this study: Sheffield ( $N = 504$ ), Aberdeen ( $N = 158$ ), Berlin ( $N = 187$ ), Kiel ( $N = 399$ ), and Paris ( $N = 466$ ). Scans are collected using either a Hologic QDR 4500A (Sheffield, Paris, and Kiel) or a GE-Lunar Prodigy scanner (Aberdeen and Berlin).

### 3.1 DXA Cross-Calibration

We validated the proposed technique using synthetic and experimental data.

**Synthetic data:** The parameters chosen to synthesise BMD measurements are as follows:  $C = 3$ ,  $N_1 = 200$ ,  $N_2 = 300$ , and  $N_3 = 100$ . The latent true BMD values were sampled randomly from a Gaussian distribution with  $\mu_0 = 1.3$  and  $\sigma_0 = 0.25$ . We tested the performance at low, medium, and high noise levels; signal-to-noise ratio (SNR) were set to 28dB, 16dB, and 8dB, respectively. A Monte Carlo procedure with 1000 iterations was conducted and the mean and the standard deviation of the estimated parameters are reported in Table 1.

**Parameter estimation:** A prospective cohort from those scanned on each machine were selected such that they were matched for gender, age, body mass index (BMI), scan side, ethnicity, and the geographical location. Fig. 4 shows the estimated calibration parameters per each pixel coordinate, i.e. the slope  $a_c$  and the intercept  $b_c$ , for the Hologic scanner.

**Table 1:** Cross-Calibration using synthetic dataset

	Ground Truth	Estimated [mean (standard deviation)]		
		SNR = 28dB	SNR = 16dB	SNR = 8dB
$a_1$	0.70	0.692(0.041)	0.703(0.042)	0.740(0.045)
$a_2$	1.40	1.392(0.055)	1.386(0.055)	1.340(0.057)
$a_3$	0.90	0.916(0.060)	0.910(0.060)	0.919(0.061)
$b_1$	0.10	0.111(0.057)	0.097(0.056)	0.047(0.060)
$b_2$	-0.30	-0.291(0.074)	-0.283(0.074)	-0.222(0.076)
$b_3$	0.20	0.180(0.079)	0.186(0.080)	0.175(0.081)

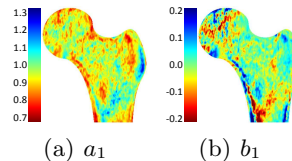


**Fig. 4:** Calibration parameters for the Hologic.

**Experimental data:** Fig. 5 demonstrates the effect of calibration on fitting quantile curves. Amalgamation of Hologic and GE-Lunar scans with no calibration enforces a distinct distortion at the age of 80s onwards where the black line tilted toward the blue line (Fig. 5(a)). Following calibration, the median curves show a consistent pattern in the standardised BMD (sBMD) space (Fig. 5(b)). The fitted curves on the standardised amalgamated dataset can be mapped back to either the Hologic or the GE-Lunar space (see Fig 5(c) and Fig. 5(d)).

### 3.2 The standardised spatio-temporal ageing atlas

We tested the RFA precision using a set of 25 scan pairs, each pair collected from the same subject on the same day with repositioning between scans. The precision expressed as the coefficient of variation (CV) at the total hip was 1.1%. Fig. 6(a) shows the constructed atlas. Cortical thinning was observed consistently

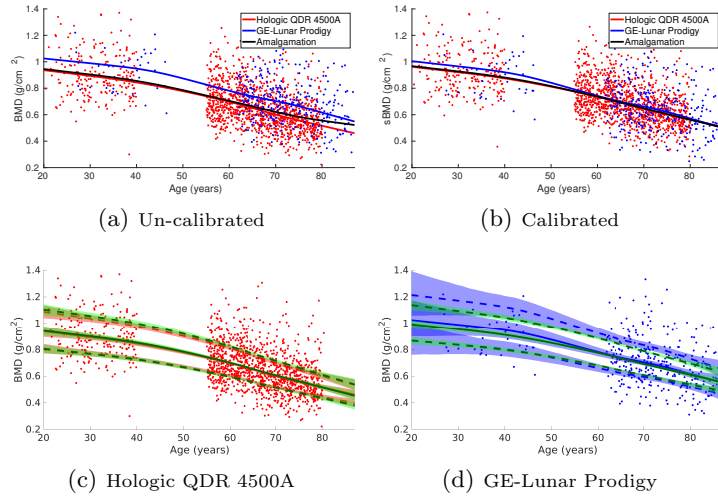


**Fig. 5:** Fitted quantile curves for the Hologic (red), the GE-Lunar (blue), or the amalgamated (black) dataset. The solid lines represent the median and the dashed lines represent the 50% quantile range. The shaded area shows the 95% confidence interval.

with ageing around the shaft from the 60s onwards. A widespread bone loss was also observed in the trochanteric area. Fig. 6(b) presents the animated atlas to visualise the gradual bone loss with ageing. Fig. 4(b-d) show quantile curves at the superior, mid, and inferior femoral neck. These curves demonstrated different rates of bone loss. Bone loss was observed consistently in the mid-femoral neck, whilst bone mass was preserved the most in the inferior femoral neck cortex.

## 4 Conclusion

This work presented the first spatio-temporal atlas of ageing bone in the femur using a large-scale multi-centre dataset ( $N=1,714$ ). We presented a region free analysis technique for DXA enabling statistical inference at the pixel level. We presented a novel cross-calibration technique to integrate data from different DXA manufacturers into an amalgamated large-scale dataset, enabling better representativeness of the estimated maps. The developed atlas provides detailed insights on spatially-complex bone loss patterns.

**Acknowledgement.** M Farzi was funded through a PhD Fellowship from Medical Research Council-Arthritis Research UK Centre for Integrated research into Musculoskeletal Ageing (CIMA).

## References

- [1] Khosla, S., Riggs, B.L.: Pathophysiology of age-related bone loss and osteoporosis. *Endocrinology and Metabolism Clinics* **34**(4) (2005) 1015–1030

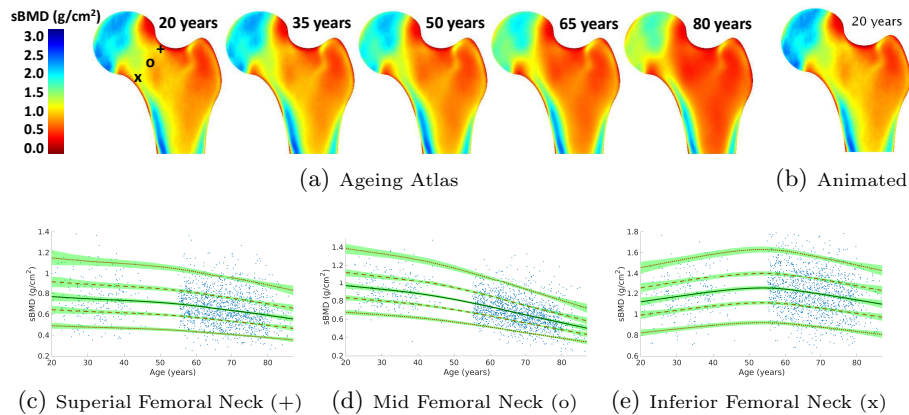


**Fig. 6:** Bone ageing atlas. (a) The median BMD maps as a function of age. (b) Animated atlas. Hover the pointer over the image and click once (Adobe Reader is required.) (c,d,e) The solid, dashed, and dotted lines show the median, the 50% and the 90% quantile ranges, respectively. The green shadow shows the 95% confidence interval.

- [2] Demontiero, O., Vidal, C., Duque, G.: Ageing and bone loss: new insights for the clinician. *Therapeutic advances in musculoskeletal disease* **4**(2) (2012) 61–76
- [3] Huizinga, W., Poot, D., Vernooij, M., et al.: A spatio-temporal reference model of the ageing brain. *NeuroImage* **169** (2017) 11–22
- [4] Adams, J.E.: Advances in bone imaging for osteoporosis. *Nature Reviews Endocrinology* **9**(1) (2013) 28–42
- [5] Genant, H.K., Grampp, S., Gluer, C.C., et al.: Universal standardization for dual x-ray absorptiometry: patient and phantom cross-calibration results. *J. Bone Miner. Res.* **9**(10) (1994) 1503–1514
- [6] Lu, Y., Ye, K., Mathur, A.K., et al.: Comparative calibration without a gold standard. *Stat. Med.* **16**(16) (1997) 1889–1905
- [7] Farzi, M., Morris, R.M., Penny, J., et al.: Quantitating the effect of prosthesis design on femoral remodeling using high-resolution region-free densitometric analysis (DXA-RFA). *Journal of Orthopaedic Research* **35**(10) (2017) 2203–2210
- [8] Lindner, C., Thiagarajah, S., Wilkinson, J.M., et al.: Fully automatic segmentation of the proximal femur using random forest regression voting. *IEEE Trans. Med. Imag.* **32**(8) (2013) 1462–1472
- [9] Goodall, C.: Procrustes methods in the statistical analysis of shape. *Journal of the Royal Statistical Society* **53**(2) (1991) 285–339
- [10] Bookstein, F.: Principal warps: Thin-plate splines and the decomposition of deformations. *IEEE Trans. Pattern Anal. Mach. Intell.* **11**(6) (1989) 567–585
- [11] Yee, T.W.: Quantile regression via vector generalized additive models. *Stat. Med.* **23**(14) (2004) 2295–2315
- [12] Carpenter, J., Bithell, J.: Bootstrap confidence intervals: when, which, what? A practical guide for medical statisticians. *Stat. Med.* **19**(9) (2000) 1141–1164
- [13] Gluer, C.C., Eastell, R., Reid, D.M., et al.: Association of five quantitative ultrasound devices and bone densitometry with osteoporotic vertebral fractures in a population-based sample: the OPUS Study. *J. Bone Miner. Res.* **19**(5) (2004) 782–93